

Estimation of OH in urban plume using TROPOMI inferred NO₂/CO

Srijana Lama¹, Sander Houweling^{1,2}, K. Folkert Boersma^{3,4}, Ilse Aben^{2,1}, Hugo A. C. Denier van der Gon⁶, Maarten C. Krol^{3,7}

¹Vrije Universiteit, Department of Earth Sciences, Amsterdam, the Netherlands

²SRON Netherlands Institute for Space Research, Leiden, the Netherlands

³Wageningen University, Meteorology and Air Quality Group, Wageningen, the Netherlands

⁴Royal Netherlands Meteorological Institute, R&D Satellite Observations, de Bilt, the Netherlands

⁶TNO, Department of Climate, Air and Sustainability, Princetonlaan, the Netherlands

⁷Institute for Marine and Atmospheric Research Utrecht, Utrecht University, Utrecht, the Netherlands

Corresponding author: Srijana Lama (s.lama@vu.nl, sreejanalama@gmail.com)

Key Points:

- A new method is proposed for estimating OH concentrations in urban plumes using TROPOMI derived NO₂/CO ratios and WRF.
- A least squares optimization method is used to optimize summer and winter OH concentrations over Riyadh.
- TROPOMI derived OH concentrations exceed model estimates from the CAMS by 32.03 % in summer and 52.0% in winter.

Abstract

A new method is presented to estimate urban OH concentrations using the downwind decay of the TROPOMI derived NO₂/CO ratio combined with Weather Research Forecast (WRF) simulations. Seasonal OH concentrations, NO_x and CO emissions for summer (June to October, 2018) and winter (November, 2018 to March, 2019) are derived for Riyadh. WRF is able to simulate NO₂ and CO urban plumes over Riyadh as observed by TROPOMI. However, WRF simulated NO₂ plumes close to center of the city are overestimated by 25 % in summer and 40 to 50 % in winter compared to TROPOMI observations. WRF simulated CO plumes differ by 10 % with TROPOMI in both seasons. The differences between model and TROPOMI are used to optimize the OH concentration, NO_x and CO emissions iteratively using a least squares method. For summer, both the NO₂/CO ratio optimization and the XNO₂ optimization imply that the OH prior from the Copernicus Atmospheric Monitoring Service (CAMS) has to be increased by $32.03 \pm 4.0\%$. The OH estimations from the NO₂/CO ratio and the XNO₂ optimization differ by 10 % indicating that the method is quite robust. Summer Emission Database for Global Atmospheric Research v4.3.2 (EDGAR) NO_x and CO emissions over Riyadh need to be increased by $42.1 \pm 8.7\%$ and $100.8 \pm 9.5\%$. For winter, the optimization method increases OH by $\sim 52.0 \pm 5.3\%$, while reducing NO_x emission by $15.45 \pm 3.4\%$ and doubling the CO emission. TROPOMI derived OH concentrations and pre-existing Exponentially Modified Gaussian function fit (EMG) method differ by 18 % in summer and 7.5 % in winter, confirming that urban OH concentrations can be reliably estimated using the TROPOMI-observed NO₂/CO ratio.

1 Introduction

The rapidly growing urbanization has led to an increase in the number of big cities globally. More than 55 % of the global population resides in cities and this fraction is projected to increase to 68% in 2050 (United Nations, 2018). The associated rise in consumption of energy and materials leads to severe air pollution, affecting the health of the large urban population (Pascal et al., 2013; Sicard et al., 2021). Air pollution control measures and the application of cleaner technology have reduced the NO₂ concentrations in developed cities such as Los Angeles and Paris by 1.5 to 3.0 % yr⁻¹ between 1996 to 2017 (Georgoulas et al., 2019). The CO emission is reduced by 28.8 % to 60.7 % in these cities in the period 2000 to 2008 (Dekker et al., 2017). In developing cities such as Tehran and Baghdad, however, nitrogen dioxide (NO₂) concentrations have increased by 8.6 % yr⁻¹ and 16.9% yr⁻¹ between 1996 to 2017 (Georgoulas et al., 2019). The CO emission increased by 15% in New Delhi in the period 2000 to 2008 (Dekker et al., 2017). As a consequence, air pollution monitoring and mitigation in developing cities is becoming an increasingly important priority.

Nowadays, urban air pollution can be studied using a combination of ground-based measurement networks and satellite observations (Ialongo et al., 2020; Sannigrahi et al., 2021). Satellite observations have helped to investigate urban air pollution, particularly in cities without a ground-based monitoring network (Beirle et al., 2019a; Borsdorff et al., 2019). In past decades, improvements in the quality and spatial resolution of satellite instruments have allowed the detection of trends in air pollutants and the quantification of urban emissions (Lorente et al., 2019; Verstraeten et al., 2018; Wennberg et al., 2018). Several studies have focused on NO_x, using NO₂ observations from the SCanning Imaging Absorption spectroMeter for Atmospheric CartographY (SCIAMACHY), the Ozone Monitoring Instrument (OMI) and TROPOMI (Ding et al., 2017; Lorente et al., 2019). At the resolution and sensitivity of TROPOMI, urban NO₂ enhancements can be detected readily, even in single satellite overpass, owing in part to the short NO₂ lifetime. OMI derived NO₂ data have been used to quantify NO_x emissions, as well as the urban lifetime of NO₂, as demonstrated by Beirle et al. (2011a) using the Exponentially Modified Gaussian function fit (EMG) method. In the EMG method, the satellite observed exponential decay of NO₂ downwind of the city centre is used to quantify the first order loss of NO₂, driven primarily by its reaction with the hydroxyl radical (OH). Liu et al. (2016) modified the EMG method for application to complex emission patterns. The quantification of CO emissions from cities is more complicated compared with NO₂ because of its longer lifetime, and the related importance of CO sources from the surroundings of cities. Nevertheless, a few studies have demonstrated the feasibility of quantifying relative changes in urban CO emission, using Measurement of Pollution in the Troposphere (MOPITT), Infrared Atmospheric Sounding Interferometer (IASI), Atmospheric Infrared Sounder (AIRS), and Tropospheric Monitoring Instrument (TROPOMI) observations (Borsdorff et al., 2019; Dekker et al., 2017; Pommier et al., 2013).

In recent years, methods have been developed that combine satellite measurements of different trace gases, for example the combined use of NO₂ and CO, to obtain specific information about pollutant sources (Lama et al., 2020; Hakkarainen et al., 2015; Miyazaki et al., 2017; Reuter et al., 2019; S. Silva & Arellano, 2017). The emission factors of CO and NO_x from fuel combustion are uncertain and vary strongly with the combustion efficiency (Flagan & Seinfeld, 1988). The satellite observed NO₂/CO ratio is particularly sensitive to this fuel burning efficiency, as demonstrated by Lama et al., (2020) and can be used to evaluate emission inventories. However, another important uncertainty arises from the removal of NO₂ by OH. In Lama et al. (2020) this OH removal is accounted for by using OH estimates from Chemical Transport Models (CTM's), which has an uncertainty of > 50 % (Huijnen et al., 2019). To reduce this uncertainty using direct measurement of OH is almost impossible due to the short lifetime, limiting the spatial representativeness of the data (de Gouw et al., 2019). The aim of this study is therefore to estimate the average OH concentration in the urban plume of large cities (hereafter referred to as urban OH) from the downwind decay of the TROPOMI observed NO₂/CO ratio. The proposed method makes use of the WRF model (Grell et al., 2005) to simulate atmospheric transport. The TROPOMI instrument (Veefkind et al., 2012), launched on 13 October 2017 on board the Sentinel-5 Precursor satellite, is particularly well suited for this task, as it measures both compounds with high sensitivity and spatial resolution. Our method uses CO, because it has a longer lifetime than NO₂ (weeks-months compared to a few hours). Therefore, CO can be considered as an inert tracer at the time-scale of urban plumes. The difference in the rate of decay between NO₂ and CO provides therefore information about the photochemical oxidation of NO₂, because atmospheric dispersion is expected to have a very similar impact on both tracers and therefore cancels out in their ratio. The use of the NO₂/CO ratio for estimating urban scale OH is further compared to the Exponentially Modified Gaussian function fit (EMG) method, using only satellite retrieved NO₂ (Beirle et al., (2011a). The city of Riyadh (24.63° N, 46.71° E) is chosen as a test case. Riyadh is an isolated city and a strong source of CO and NO₂ pollution (Beirle et al., 2019; Lama et al., 2020). The frequent clear sky conditions over Riyadh yield a large number of valid TROPOMI CO and NO₂ data. The signal to noise in TROPOMI is high enough to detect the enhancement of CO and NO₂ over Riyadh in a single overpass (Lama et al., 2020). Model results from the Copernicus Atmospheric Monitoring Service (CAMS) for Riyadh show a distinct seasonality in OH (see Fig S1), which we attempt to evaluate using TROPOMI data for summer and winter. This paper is organized as follows: Section 2 describes the TROPOMI NO₂ and CO data, the WRF model setup that was used, and the optimization method that is used for estimating OH. Optimization results and comparisons between TROPOMI and WRF are presented in section 3, followed by a summary and conclusion of the main finding in section 4. Additional figures and information about the optimization method are provided in the Supplement.

2. Data and Method

2.1 TROPOMI NO₂ tropospheric column

We used the offline TROPOMI level 2 tropospheric column NO₂ [mole m⁻²] data from retrieval versions 1.2.x for 2018 and 1.3.x for 2019 available at <https://s5phub.copernicus.eu>; <http://www.tropomi.eu> (last access: 21 September, 2020). NO₂ data of versions 1.2.x and 1.3.x have minor processing differences such as removal of negative cloud fraction, better flagging and uncertainty estimation. However, they use the same retrieval algorithm applied to level-1b version 1.0.0 spectra (Babic et al., 2017) recorded by the TROPOMI UV-Vis module in the 405-465nm spectral range. The TROPOMI NO₂ DOAS software, developed at KNMI, is used for the processing of NO₂ slant column densities (van Geffen et al., 2019). The improved NO₂ DOMINO algorithm of Boersma et al. (2018) has been used to translate slant columns into tropospheric column densities. In this algorithm, stratospheric contributions are subtracted from the slant column densities and the residual tropospheric slant column density is converted to tropospheric vertical column density using the air mass factor (AMF). The AMF depends on the surface albedo, terrain height, cloud height and cloud fraction (Eskes et al., 2018; Lorente et al., 2017). The comparison of MAX-DOAS ground based measurements in European cities shows that TROPOMI underestimates of NO₂ columns by 7% to 29.7 % (Lambert et al., 2019). To avoid biases, we re-calculated the AMF by replacing the tropospheric AMF, which is based on a vertical NO₂ column simulated by TM5, with the WRF-chem equivalent (Boersma et al., 2016;

Lamsal et al., 2010; Visser et al., 2019), using the equation provided in the Appendix A. During summer, the bias correction increases TROPOMI XNO₂ by 5 to 10 % and in winter by 25% to 30 % in the urban plume over Riyadh, whereas background areas are less affected (see Fig S2).

2.2 TROPOMI CO

For CO, the offline level 2 CO data product version 1.2.2 has been used, available at <https://cophub.copernicus.eu/s5pexp> (last access: 20 September, 2020). The SICOR algorithm is applied to TROPOMI 2.3 µm spectra to retrieve CO total column density [molec cm⁻²] (Landgraf et al., 2016). The retrieval method is based on a profile scaling approach, in which TROPOMI-observed spectra are fitted by scaling a reference vertical profile of CO using the Tikhonov regularization technique (Borsdorff et al., 2014). The reference CO profile is obtained from the TM5 transport model (Krol et al., 2005). The averaging kernel (A) quantifies the sensitivity of the retrieved total CO column to variations in the true vertical profile (ρ_{true}), as follows (Borsdorff et al., 2018a):

$$C_{\text{retrieval}} = A \cdot \rho_{\text{true}} + \epsilon_{\text{CO}} \quad (1)$$

where, $C_{\text{retrieval}}$ is the retrieved column average CO mixing ratio, ϵ_{CO} is the retrieval error, statistically represented by the retrieval uncertainty that is provided for each CO retrieval.

2.3 Satellite Data Selection and Filtering Criteria

As NO₂ and CO are retrieved from different channels of TROPOMI using different retrieval algorithms, the filtering criteria and spatial resolutions of CO and NO₂ are different. The data filtering makes use of the quality assurance value (qa) and is provided with the CO and NO₂ retrievals, ranging from 0 (no data) to 1 (high quality data). We selected NO₂ retrievals with $qa \geq 0.75$ (clear sky condition) and CO retrievals with $qa \geq 0.7$ (clear sky or low level cloud) as in Lama et al., (2020). The SICOR algorithm was originally developed for SCIAMACHY to account for the presence of low elevation clouds, increasing the number of valid measurements (Borsdorff et al., 2018a). In addition, the CO stripe filtering technique is applied as described by Borsdorff et al. (2018). Using dry air column density derived from the surface pressure data in CO and NO₂ TROPOMI files, the total CO column and tropospheric NO₂ column densities are converted to dry column mixing ratios XCO (ppb) and XNO₂ (ppb). The spatial resolution of the NO₂ data is finer compared to the CO data (3.5x7 km² versus 5.5x7 km²). After the CO and NO₂ retrievals pass the filtering criteria, their co-location is approximated by assigning the centre coordinates of an NO₂ retrieval to the CO footprint in which it is located (Lama et al., 2020).

2.4 Weather Research Forecast (WRF)

We have used WRF (<http://www.wrf-model.org/>), version 3.9.1.1 to simulate NO₂ and CO mixing ratios over Riyadh. WRF is a non-hydrostatic model designed by the National Center for Environmental Protection (NCEP) for both atmospheric research and operational forecasting applications. For this study, we have setup three nested domains in the model at resolutions of 27 km, 9 km and 3 km, centred at 24.63°N, 46.71°E. The first and second domain cover Saudi Arabia and provide the boundary conditions for the nested third domain (see Fig. S3). The analysis in this paper uses the 500 x 500 km² sub region around Riyadh in the third domain, containing 161 by 161 grid cells. All domains are extended vertically from the Earth's surface to 50 hPa, using 31 vertical layers, with 17 layers in the lowermost 1500 m. WRF simulations are performed using a time step of 90 seconds for the period June 2018 to March 2019, using a spin-up time of 10 days.

We have used the Unified Noah land surface model for surface physics (Ek et al., 2003; Tewari et al., 2004), an updated version of the Yonsei University (YSU) boundary layer scheme (Hu et al., 2013) for the boundary layer processes, and the Rapid Radiative Transfer Method (RRTM) for short-wave and long-wave radiation (Mlawer et al., 1997). Cloud physics is solved with the new Tiedtke cumulus parameterization scheme (Zhang & Wang, 2017). The WRF Single Moment 6-class scheme is used for microphysics (Hong & Lim, 2006). The WRF coupling with chemistry (WRF-chem) allows the simulation of tracer transport and the chemical transformation of trace gases and

aerosols. Here, we used the passive tracer transport function instead of the encoded chemistry in WRF to speed up the model simulation. In addition, the passive tracer option helps in separating the influences of wind, OH and the rate constant of the $\text{NO}_2 + \text{OH}$ reaction ($K_{\text{NO}_2, \text{OH}}$) on the NO_2/CO ratio in the downwind city plume. The function of different tracers, their acronym and explanation of different WRF simulations is provided in Table 1.

Table 1. Summary of WRF simulations and the definition of tracers and acronym used.

| WRF Simulation / Tracer | WRF input / Tracer definition |
|--|--|
| Prior | WRF run using NCEP meteorological data, EDGAR CO and NO_x emissions, CAMS OH, and CAMS CO and NO_x as initial and lateral boundary conditions. |
| $\text{WRF}_{\text{OH} \times 1.1}$ | Prior run with CAMS OH increased by 10 % |
| Optimized run _{1st iter} | Optimized state (background, emission, OH) after iteration 1 |
| Optimized run _{2nd iter} | Optimized state (background, emission, OH) after iteration 2 |
| CO | |
| XCO_{emis} | The contribution of urban CO emissions to XCO |
| XCO_{Bg} | The contribution of the background to XCO |
| XCO_{WRF} | XCO from the Prior run |
| $\text{XCO}_{\text{WRF}, 1\text{st iter}}$ | XCO from Optimized run _{1st iter} |
| $\text{XCO}_{\text{WRF}, \text{opt}}$ | XCO from Optimized run _{2nd iter} |
| NO_2 | |
| $\text{XNO}_2 \text{ emis}$ | The contribution of urban NO_x emissions to XNO_2 , ignoring the OH sink |
| $\text{XNO}_2 (\text{emis}, \text{OH})$ | As $\text{XNO}_2 (\text{emis}, \text{OH})$ accounting for the OH sink |
| $\text{XNO}_2 (\text{emis}, \text{OH} \times 1.1)$ | As $\text{XNO}_2 (\text{emis}, \text{OH})$ with CAMS OH increased by 10% |
| $\text{XNO}_2 \text{ Bg}$ | The contribution of the background to XNO_2 |
| $\text{XNO}_2 \text{ WRF}$ | XNO_2 from the Prior run. |
| $\text{XNO}_2 (\text{WRF}, \text{OH} \times 1.1)$ | XNO_2 from $\text{WRF}_{\text{OH} \times 1.1}$. |
| $\text{XNO}_2 \text{ WRF } 1\text{st iter}$ | XNO_2 from Optimized run _{1st iter} |
| $\text{XNO}_2 \text{ WRF opt}$ | XNO_2 from Optimized run _{2nd iter} |
| Ratio (NO_2/CO) | |
| Ratio _{without OH} | Ratio of $\text{XNO}_2 \text{ emis}$ and XCO_{emis} |
| Ratio _{with OH} | Ratio of $\text{XNO}_2 (\text{emis}, \text{OH})$ and XCO_{emis} |
| Ratio _{Bg} | Ratio of $\text{XNO}_2 \text{ Bg}$ and XCO_{Bg} |
| WRF Ratio | Ratio of $\text{XNO}_2 \text{ WRF}$ and XCO_{WRF} |
| WRF Ratio _{$\text{OH} \times 1.1$} | Ratio of $\text{XNO}_2 (\text{WRF}, \text{OH} \times 1.1)$ and XCO_{WRF} |
| WRF Ratio _{1st iter} | Ratio of $\text{XNO}_2 \text{ WRF } 1\text{st iter}$ and $\text{XCO}_{\text{WRF}, 1\text{st iter}}$ |
| WRF Ratio _{opt} | Ratio of $\text{XNO}_2 \text{ WRF}, \text{opt}$ and $\text{XCO}_{\text{WRF}, \text{opt}}$ |

The meteorological initial and boundary conditions are based on NCEP data at $1^\circ \times 1^\circ$ spatial and 6-hr temporal resolution available at <https://rda.ucar.edu/datasets/ds083.2/>. Nitrogen Oxides ($\text{NO}_x = \text{NO}_2 + \text{NO}$) and CO anthropogenic emissions have been taken from the Emission Database for Global Atmospheric Research v4.3.2 (EDGAR) 2012 at $0.1^\circ \times 0.1^\circ$ spatial resolution (Crippa et al., 2016). Note that recently also EDGAR v5 2015 (Crippa et al., 2020) has been made available at https://edgar.jrc.ec.europa.eu/index.php/dataset_ghg50, but these new data are not used in this study. The EDGAR 2012 data has been re-gridded to the resolution of the WRF domains and hourly, weekly and monthly emission variations are taken into account using the temporal emission factors provided by van der Gon et al. (2011). The chemical boundary conditions for CO and NO_x are based on the CAMS chemical reanalysis product at $0.75^\circ \times 0.75^\circ$ spatial, and 3-hourly temporal resolution (Inness et al., 2019), retrieved from

<https://ads.atmosphere.copernicus.eu/cdsapp#!/dataset/cams-global-reanalysis-eac4?tab=form>, last access: 1st November, 2020). XCO and XNO₂ boundary condition based on CAMS is assumed to be representative as background value within the domain. Since we do not explicitly compute the sources and sinks of background NO₂ inside the domain, we decide to transport the boundary conditions as background passive tracers.

The conservative transport in WRF causes the influence of NO_x and CO emissions from Riyadh on their column average mixing ratios to be linear. For chemistry, we only consider the first-order loss of NO_x by the hydroxyl radical (OH) converting nitrogen dioxide (NO₂) to nitric acid (HNO₃). Note that in this study, OH is only applied to the urban NO_x emission tracer (XNO_x(emis,OH)). The CAMS NO_x background tracer (XNO_xBg) is transported in WRF without OH decay, since it already represents the balance between regional sources and sinks. CAMS hydroxyl radical (OH) data at a resolution of 0.75°x0.75° spatial and 3 hourly temporal resolution (Inness et al., 2019) retrieved at <https://ads.atmosphere.copernicus.eu/cdsapp#!/dataset/cams-global-reanalysis-eac4?tab=form>, last access: 1st July, 2020) is spatially, temporally and vertically interpolated to the WRF grid. The NO_x lifetime is derived as follows:

$$\frac{d\text{NO}_x}{dt} = \frac{d\text{NO}_2}{dt} = K_{\text{NO}_2\text{OH}} \cdot \text{OH} \cdot \text{NO}_2 \quad (2)$$

$$\text{fact} = \frac{\text{NO}_x}{\text{NO}_2} \quad (3)$$

$$\tau_{\text{NO}_x} = \frac{1}{\frac{K_{\text{NO}_2\text{OH}}}{\text{fact}} \cdot \text{OH}} \quad (4)$$

where, $K_{\text{NO}_2\text{OH}}$ is the International Union of Pure and Applied Chemistry (IUPAC) 2nd order rate constant for the reaction of NO₂ with OH [REF?]. “fact” represents the fractional contribution of NO₂ to NO_x (NO_x/NO₂). This NO_x to NO₂ conversion factor is derived from the CAMS reanalysis and re-gridded to WRF, to account for its spatial and temporal variation. τ_{NO_x} is the lifetime of NO_x.

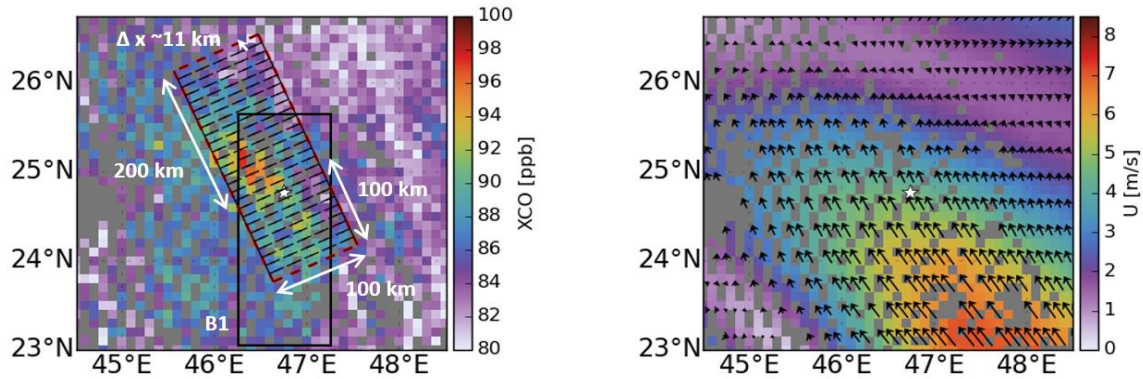


Figure 1. TROPOMI derived XCO (left) and average wind speed and wind direction from the surface to the top of boundary layer derived from the CAMS global reanalysis eac4 data at the TROPOMI overpass time over Riyadh for August 4th, 2018. The white star represents the centre of Riyadh. The black box (B1) with a dimension of 300 x 100 km² is rotated in the average wind direction at 50 km radius from the centre of Riyadh at the TROPOMI overpass time resulting in the red box. For the calculation of cross-directional averaged NO₂ and CO, the red box is divided into 29 smaller cells with the width (Δx) ~11 km. For this TROPOMI derived XCO is gridded at 0.1°x0.1°.

In earlier work with satellite NO₂ data, the Jet Propulsion Laboratory (JPL) high pressure limit was used as rate constant to represent the first order loss of NO₂ (Beirle et al., 2011; Lama et al., 2020; Lorente et al., 2019). However, we found this approximation to be too crude, and therefore apply the full IUPAC recommended pressure dependent formula for the 2nd order rate constant. Supplement Figure S4 shows the difference between the three rate constants,

i.e. JPL high pressure limit, JPL 2nd order and IUPAC 2nd order, confirming the importance of accounting for the pressure dependence.

WRF output for the third domain is interpolated spatially and temporally to the footprints of TROPOMI. The interpolated WRF- NO_x tracers are converted to NO₂ using the conversion factor derived from the CAMS reanalysis accounting for its spatial and temporal variation (for the names and functions of tracers see Table 1). The averaging kernel available for each TROPOMI CO and NO₂ observation is applied to the WRF output, after interpolation to the vertical layers of the TROPOMI retrieval. To compare WRF output to TROPOMI, WRF derived XNO₂ (XNO₂_{WRF}) is calculated by combining the NO₂ emission tracer that accounts for the OH effect (XNO₂_(emis,OH)) and the CAMS NO₂ background (XNO₂_{Bg}) (see Fig. S5 and S6). Similarly, the CO emission tracer (XCO_{emis}) is added to the CAMS CO background (XCO_{Bg}) to calculate WRF simulated XCO (XCO_{WRF}) (see Fig. S7 and S8).

2.5 NO₂/CO ratio calculation using box rotation

The variation of the NO₂/CO ratio in the downwind city plume is calculate as a function of distance x from the city centre in downwind direction. We select days with an average wind speed (U) in the range of 3.0 m/s (Beirle et al., 2011a) $< U < 8.5$ m/s (Valin et al., 2013) within a 50 km radius from the centre of Riyadh (24.63° N, 46.71° E). The horizontal distribution of EDGAR emissions over Riyadh is used within this 50 km radius (Fig S9). Ninety five days in summer and 70 days in winter meet the wind speed criteria over Riyadh for the ratio calculation. The boundary layer average wind speed and direction is calculated using the CAMS global reanalysis eac4 (retrieved at <https://ads.atmosphere.copernicus.eu/cdsapp#!/dataset/cams-global-reanalysis-eac4?tab=form>, last access : 1st August, 2020) at a resolution of 0.75°x0.75° spatial and 3 hourly temporal resolution. For this, the CAMS wind vector is spatially and temporally interpolated to the central coordinate of TROPOMI pixels.

To compute the NO₂/CO ratio as function of the downwind distance x , TROPOMI and WRF data have been re-gridded at 0.1°x0.1°. A box (B1) is selected with a width of 100 km, from 100 km in upwind to 200 km in downwind direction of the city centre (see Fig 1a). The dimension of the box is motivated by multiple TROPOMI overpasses over Riyadh showing NO₂ and CO enhancements advected downwind over a ~200 km distance, without other large sources of NO₂ and CO within a 100 km radius of the city centre (see Fig. 1a). Figure 1(b) shows the boundary layer averaged wind speed and wind direction over Riyadh indicating flow towards the northeast on 4th of August, 2018. The box is rotated for every TROPOMI overpass depending upon the daily average wind direction within a 50 km radius from centre of Riyadh as shown in Figure 1(a) and Figure S10. The rotated box B1 is divided into N rectangular boxes, orthogonal to the wind direction with length (Δx) ~11 km (see Fig. 1 and Fig. S10). The XNO₂ and XCO grid cells that fall within the N rectangular boxes are selected to derive zonally averaged XNO₂ and XCO for summer and winter.

Unlike the enhancements over the city, ΔXNO_2 and ΔXCO become smaller than retrieval uncertainties at large distance from the city, where the ratio $\Delta XNO_2/\Delta XCO$ becomes ill-defined. Therefore, we decided to use the ratio of mean XNO₂ and XCO instead of enhancements over the background. To analyse the influence of atmospheric transport and the OH sink on the WRF derived XNO₂/XCO ratio two different ratios are derived: 1. $\frac{XNO_2_{emis}}{XCO_{emis}}$, named

“Ratio_{without OH}”, 2. $\frac{XNO_2_{(emis,OH)}}{XCO_{emis}}$, named “Ratio_{with OH}” (see Table 1). The CAMS background accounts for the balance between regional source and sink in CTMs so it is excluded to analyze the influence of atmospheric transport on the ratio. For the comparison between TROPOMI and WRF, the CAMS backgrounds are included in “WRF RATIO” ($\frac{XNO_2_{WRF}}{XCO_{WRF}}$) (see Table 1). The comparison of WRF RATIO to TROPOMI ratio, and the contribution of its components, is presented in section 3.2.

2.6 OH estimation: satellite data only

In the EMG method, following Beirle et al. (2011), 2D NO₂ column densities maps are assigned to eight equal wind sectors, spanning 360 degree for summer and winter. 1D column densities per wind sector are computed by averaging in cross wind direction. This way, average NO₂ column density functions of the downwind distance to the city centre

have been constructed for summer and winter (see Fig. S11). Using the EMG method as in Beirle et al., (2011), the e-folding distance x_0 and NO_2 emissions have been estimated. The NO_2 lifetime is derived by dividing x_0 by the average wind speed (5.46 m/s and 5.24 m/s for winter and summer, respectively) and is provided in Table 2. The OH concentration is derived from the inferred NO_2 lifetime using the IUPAC second order rate constant (for details see section S2 and S3). Using equation 4, the NO_x life time is derived. EMG derived NO_2 emissions are also converted to NO_x emissions using the CAMS-derived conversion factor. Summer and winter averaged CAMS derived conversion factors for the box of 300km x 100km are 1.28 and 1.31, respectively.

2.7 OH estimation: WRF optimization

To jointly estimate the NO_x and CO emissions as well as the OH concentration from the TROPOMI data, a least squares optimization method is used. This method fits the model to the data by minimizing a cost function (J) (see S1 for details). The reaction of NO_2 with OH introduces a non-linearity in the OH optimization. To account for this non-linearity, we linearize the problem around the a priori starting point, using small perturbations (10%) $\Delta\text{background}$, $\Delta\text{emission}$, ΔOH . The non-linear model is fitted to the observations, by optimizing scaling factors f_{Bg} , f_{emis} , f_{OH} to the perturbation functions $\Delta\text{background}$, $\Delta\text{emission}$ and ΔOH , respectively. This process is repeated iteratively, updating the linearization point and re-computing the perturbation functions.

We estimate OH by optimizing WRF with TROPOMI in two ways 1) optimizing the simulated NO_2/CO ratio using TROPOMI-derived ratios, named as “Ratio optimization” and 2) optimizing NO_2 and CO separately using TROPOMI derived XCO and XNO_2 named as “Component wise optimization”. First the ratio optimization is described followed by the component wise optimization. Optimized ratios are derived as follows:

$$F_{\text{TROPOMI}} = F + \frac{\Delta F}{\Delta\text{emis}} * \frac{f_{\text{emis}}}{10} + \frac{\Delta F}{\Delta\text{OH}} * \frac{f_{\text{OH}}}{10} + \frac{\Delta F}{\Delta\text{Bg}} * \frac{f_{\text{Bg}}}{10} \quad (5)$$

$$F = \frac{\text{XNO}_2_{\text{WRF}}}{\text{XCO}_{\text{WRF}}}$$

$$\text{XNO}_2_{\text{WRF}} = \text{XNO}_2_{(\text{emis},\text{OH})} + \text{XNO}_2_{\text{Bg}} \quad (6)$$

$$\text{XCO}_{\text{WRF}} = \text{XCO}_{\text{emis}} + \text{XCO}_{\text{Bg}} \quad (7)$$

$$\frac{\Delta F}{\Delta\text{emis}} = \frac{\text{XNO}_2_{(\text{emis},\text{OH})} * 1.05 + \text{XNO}_2_{\text{Bg}}}{\text{XCO}_{\text{emis}} * 0.95 + \text{XCO}_{\text{Bg}}} - F \quad (8)$$

$$\frac{\Delta F}{\Delta\text{OH}} = \frac{\text{XNO}_2_{(\text{emis},\text{OH}*1.1)} + \text{XNO}_2_{\text{Bg}}}{\text{XCO}_{\text{emis}} + \text{XCO}_{\text{Bg}}} - F \quad (9)$$

$$\frac{\Delta F}{\Delta\text{Bg}} = \frac{\text{XNO}_2_{(\text{emis},\text{OH})} + \text{XNO}_2_{\text{Bg}} * 1.05}{\text{XCO}_{\text{emis}} + \text{XCO}_{\text{Bg}} * 0.95} - F \quad (10)$$

Here, F_{TROPOMI} is the TROPOMI derived NO_2/CO ratio, F is the WRF Ratio, $\frac{\Delta F}{\Delta\text{emis}}$ is the change in F due to an increase in the NO_2 emission by 5 % and a decrease in the CO emission by 5 % ($1.05/0.95 = \sim 10\%$), $\frac{\Delta F}{\Delta\text{OH}}$ is the change in F due to an increase in OH by 10 % and $\frac{\Delta F}{\Delta\text{Bg}}$ is the change in F due to an increase in the XNO_2 background by 5 % and a decrease in the CO background by 5 %. $\text{XNO}_2_{(\text{emis},\text{OH})}$ is the contribution of city NO_x emissions to XNO_2 accounting for the OH sink, XNO_2_{Bg} is the NO_2 background. XCO_{emis} is the contribution of the EDGAR city CO emissions to XCO and XCO_{Bg} is the CO background derived from CAMS. $\text{XNO}_2_{\text{WRF}}$ and XCO_{WRF} is the WRF

derived XNO_2 and XCO respectively. $XNO_2_{(emis,OH*1.1)}$ is the contribution of city NO_x emissions to XNO_2 after increasing CAMS OH by 10 %.

Although the ratio optimization is sensitive to the emission ratio and the OH sink of NO_2 , it is not sensitive to the absolute emissions of CO and NO_2 . Therefore, we performed component-wise optimizations for XCO and XNO_2 to optimize absolute emissions. We also compare the OH factor obtained from the ratio optimization and component-wise optimization to test the robustness of the method. The optimized XNO_2 is derived using equation 11. XCO is optimized using the same equation but without considering the OH sink (see Appendix B).

$$XNO_2_{TROPOMI} = XNO_2_{WRF} + \Delta XNO_2_{emis} * \frac{f_{emis}}{10} + \Delta XNO_2_{OH} * \frac{f_{OH}}{10} + \Delta XNO_2_{Bg} * \frac{f_{Bg}}{10} \quad (11)$$

$$\Delta XNO_2_{emis} = XNO_2_{(emis,OH)} * 1.10 - XNO_2_{(emis,OH)} \quad (12)$$

$$\Delta XNO_2_{OH} = XNO_2_{(emis,OH*1.1)} - XNO_2_{(emis,OH)} \quad (13)$$

$$\Delta XNO_2_{Bg} = XNO_2_{Bg} * 1.10 - XNO_2_{Bg} \quad (14)$$

Here, $XNO_2_{TROPOMI}$ is the TROPOMI derived XNO_2 , XNO_2_{WRF} is the WRF XNO_2 . ΔXNO_2_{emis} is the change in XNO_2 due to an increase in emission by 10 %, ΔXNO_2_{OH} is change in XNO_2 due to an increase in CAMS OH by 10 % and ΔXNO_2_{Bg} is a change in the background XNO_2 by 10 %.

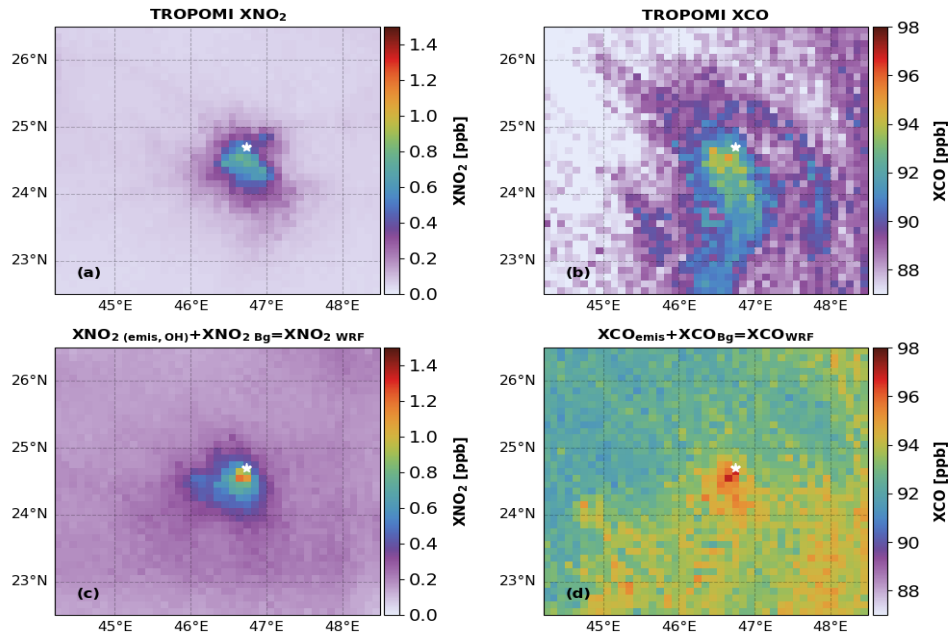


Figure 2. Comparison between XNO_2 (left) and XCO (right) from TROPOMI and WRF over Riyadh averaged over June to October, 2018. Top panels show TROPOMI data and bottom panels the corresponding co-located WRF results. XNO_2_{WRF} is derived by adding $XNO_2_{(emis,OH)}$ and XNO_2_{Bg} . XCO_{WRF} is derived by adding XCO_{emis} and XCO_{Bg} . The white star represents the centre of city. TROPOMI and WRF results are gridded at $0.1^\circ \times 0.1^\circ$.

3. Results and Discussion

3.1. XNO₂ and XCO over Riyadh

In this subsection, we compare WRF-derived XCO_{WRF} and XNO_{2 WRF} with TROPOMI for summer (see Fig. 2) and winter (see Fig. S6) over Riyadh. TROPOMI and WRF derived XCO and XNO₂ are averaged from June to October 2018 for summer and November 2018 to March 2019 for winter in a domain of 500 x 500 km² centered around Riyadh. The comparison for summer in Figure 2 shows bias-corrected TROPOMI NO₂ after replacing the TM5-based tropospheric AMF with WRF profiles as described in Visser et al. (2019). The enhancement of XNO₂ and XCO over Riyadh due to urban emissions is clearly separated from the background for TROPOMI and WRF, showing that the city of Riyadh is well suited to investigate the use of the NO₂/CO ratio to quantify OH in urban plumes. Due to the longer life-time of CO, the TROPOMI-observed XCO plume extends further in the southeast direction compared to XNO₂. Figure 2 shows that our WRF simulations are able to reproduce the TROPOMI retrieved XNO₂ ($r^2 = 0.96$) and XCO ($r^2 = 0.78$) plumes, confirming that WRF-derived $\frac{XNO_{2 WRF}}{XCO_{WRF}}$ is suitable for the optimization of CTM-derived OH concentrations using TROPOMI data. XNO_{2 WRF} is higher by 25 % compared to TROPOMI in the city centre. In the background, XCO_{WRF} shows a similar spatial distribution as TROPOMI XCO, but the values are higher by 5 to 10 % (see Fig 2.). Close to the city centre, XCO_{WRF} is ~5.7 % higher than TROPOMI XCO. In EDGAR 2011, emission sources are located in the centre of Riyadh (see Fig. S9). However, as noted by Beirle et al. (2019) they extend to a larger part of the city in reality. This difference in spatial distribution leads to higher XNO_{2 WRF} and XCO_{WRF} close to centre of Riyadh compared to TROPOMI.

In winter, the wind direction is predominantly from the south easterly sector in WRF and TROPOMI (see Fig S12). The spatial distribution of XCO_{WRF} ($r^2 = 0.73$) and XNO_{2 WRF} ($r^2 = 0.88$) matches quite well with TROPOMI. Therefore, the difference between summer and winter should offer the opportunity to quantify the seasonality in emissions and OH concentrations over Riyadh. In winter, XCO_{WRF} is ~5 to 10 % higher than TROPOMI, while XNO_{2 WRF} is higher by 40 % to 50 %. The difference could either point to uncertainties in the emission NO₂/CO emission ratio, uncertainties in the NO₂ lifetime, or inaccuracies in the background. By quantifying OH, we can evaluate these explanations (see section 3.3). XNO_{2 WRF} is higher by 20 % in winter than in summer. Contrary, TROPOMI NO₂ is lower by ~30 % in winter (Fig S12.) compared to summer (Fig. 2). Again, to disentangle the role of changing sources and sinks, we need an independent estimates of OH.

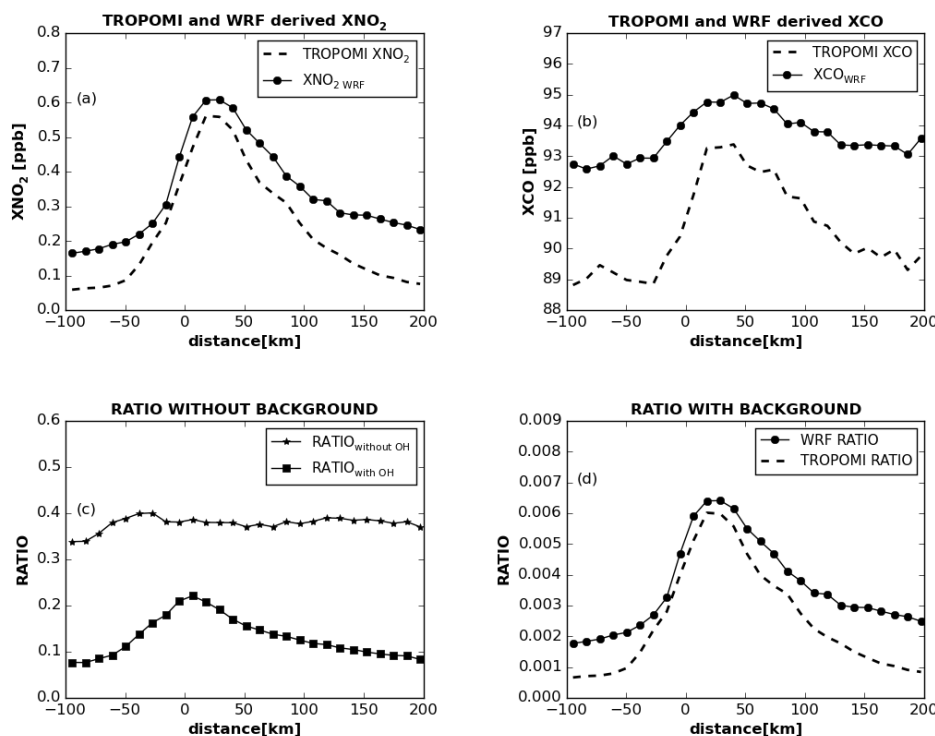


Figure 3. Comparison of WRF and TROPOMI zonally averaged a) XNO₂, b) XCO and c) WRF Ratio (XNO₂/XCO) without CAMS background d) TROPOMI and WRF Ratio (XNO₂/XCO) with background as a function of distance to the centre of Riyadh for summer (June, 2018 to October, 2019).

3.2. The XNO₂/XCO ratio and OH

Before comparing TROPOMI and WRF-derived XNO₂/XCO ratios, we first analyse the influence of atmospheric transport and the OH sink on the WRF derived XNO₂/XCO ratio. To do this three ratios are used 1. Ratio_{without OH} 2. Ratio_{with OH} 3. WRF RATIO (see Table 1). As seen in Figure 3, S13 and S14, WRF is able to reproduce the TROPOMI-observed downwind evolution of XNO₂ and XCO in summer and winter. The peak of the XNO₂ and XCO plumes is shifted away from the city centre due to the balance between the accumulation of urban emissions in the atmospheric column and atmospheric transport (Lorente et al., 2019).

As expected, Ratio_{without OH} shows an approximately straight line when the background is removed, because transport influences NO₂ and CO in the same way and therefore cancels out in the ratio (see Fig. 3b). The Ratio_{with OH} however, shows an approximately Gaussian relation with distance due to the influence of the sink on NO₂. This comparison demonstrates the sensitivity of the relation between XNO₂/XCO ratio and downwind distance to the NO₂ lifetime, which we want to exploit to quantify OH. When including the background, the shapes of the functions in Figure 3c change (not shown), because the relative weights of the background and city contributions to the ratio vary with distance of the city centre. In summer, the WRF RATIO is higher by ~15 % close to centre of city TROPOMI due to the overestimation of XNO₂ WRF in WRF (see Fig. 3d). However in the downwind plume, at a distance of 100 km WRF RATIO is higher by 20 to 50 % compared to TROPOMI.

In winter, Ratio_{without OH} and Ratio_{with OH} show relations with downwind distance that are similar to summer, confirming that an OH sink leads to a Gaussian structure of the ratio (see Fig. S14). The winter WRF RATIO is 49 % higher than TROPOMI due to the overestimation of XNO₂ by 40 to 50 %. The WRF RATIO close to the centre of

city is also 20% higher in winter than in summer, due to higher winter $\text{XNO}_2_{\text{WRF}}$ than in summer (see Fig S12 and S15). In contrast, TROPOMI shows a higher ratio in summer compared to winter (see Fig S15). These differences between TROPOMI and WRF-derived ratios offer an opportunity to address uncertainties in CTM computed urban OH and emission inventories, which will be explored next.

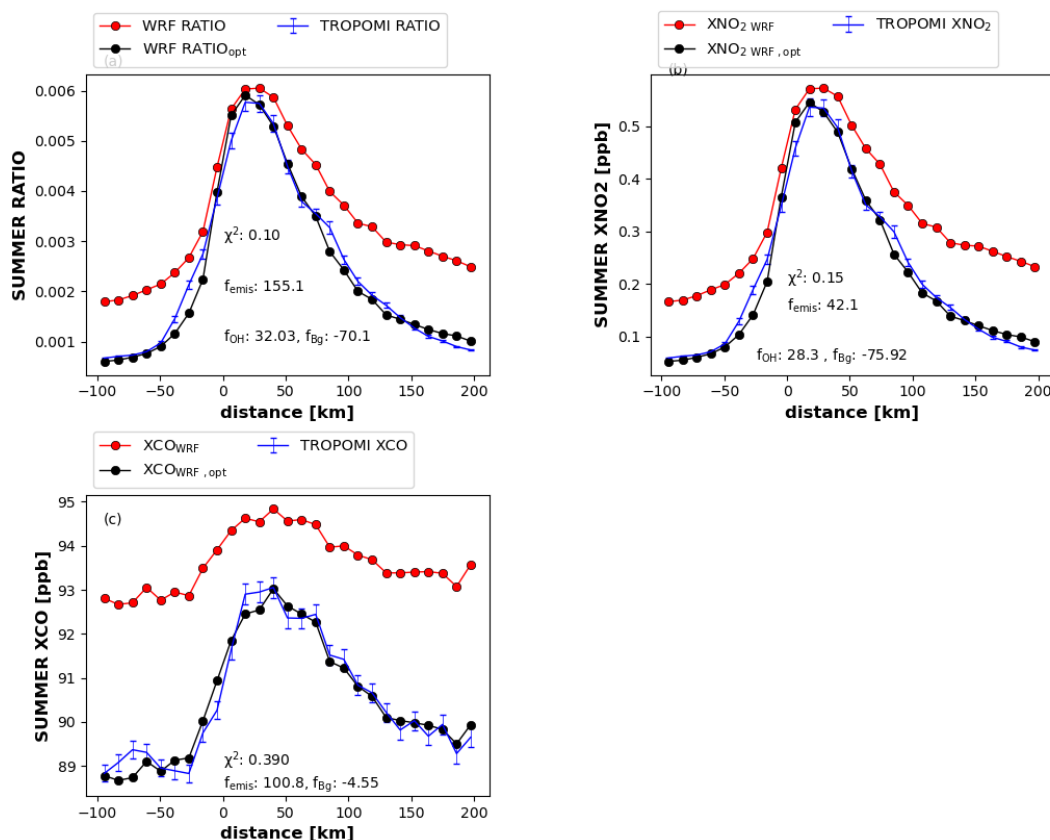


Figure 4. Comparison between TROPOMI and WRF, before and after optimization for Summer (averaged over June to October, 2018). a) XNO_2/XCO ratio, b) XNO_2 and c) XCO in comparison to TROPOMI. f_{OH} , f_{emis} and f_{Bg} are optimized scaling factors obtained iteratively for OH, emissions and background by least square optimization method. f_{emis} , f_{OH} and f_{Bg} are derived by accounting the total change in emission, OH and background using the corresponding scaling factors obtained from 1st and 2nd iterative step. The unit of scaling factor is in percent (%).

3.3 WRF optimization

To translate the discrepancies between TROPOMI and WRF derived ratios of section 3.2 into implied differences in emissions and OH, the least squares optimization method has been used as described in section 2.6. Before optimizing WRF using TROPOMI, pseudo data experiments in WRF have been carried out to test if the optimization method is capable of recovering true emissions and OH levels. To this end, changes in OH concentrations, emissions and background by known scaling factors have been applied to the WRF prior simulation to create a synthetic dataset. This process is repeated multiple times to create thousands of synthetic datasets. Subsequently, the scaling factors are obtained in the inversion procedure. These tests reveal that the estimation errors for f_{emis} , f_{OH} and f_{Bg} are less than 2.5 % (see Fig. S16). This confirms that the least square optimization method works, with two iterations leading to a sufficient accuracy, and can be used to estimate emissions and OH from TROPOMI data. Using TROPOMI data, estimation errors for f_{emis} , f_{OH} and f_{Bg} are expected to be higher due to atmospheric transport errors, simplified chemistry, and XCO and XNO₂ retrieval uncertainties. These errors did not play a role in the pseudo-data experiments, in which perfect transport and sampling was assumed. The results for summer are summarized in Figure 4, showing the optimized fit to the TROPOMI data as well as the corresponding scaling factors f_{emis} , f_{OH} and f_{Bg} that are estimated. The optimized emission, OH and Bg obtained from 2nd iteration is divided by Prior to derive the f_{emis} , f_{OH} and f_{Bg} . The results of iterative step for summer and winter is shown in Fig S17 and S18.

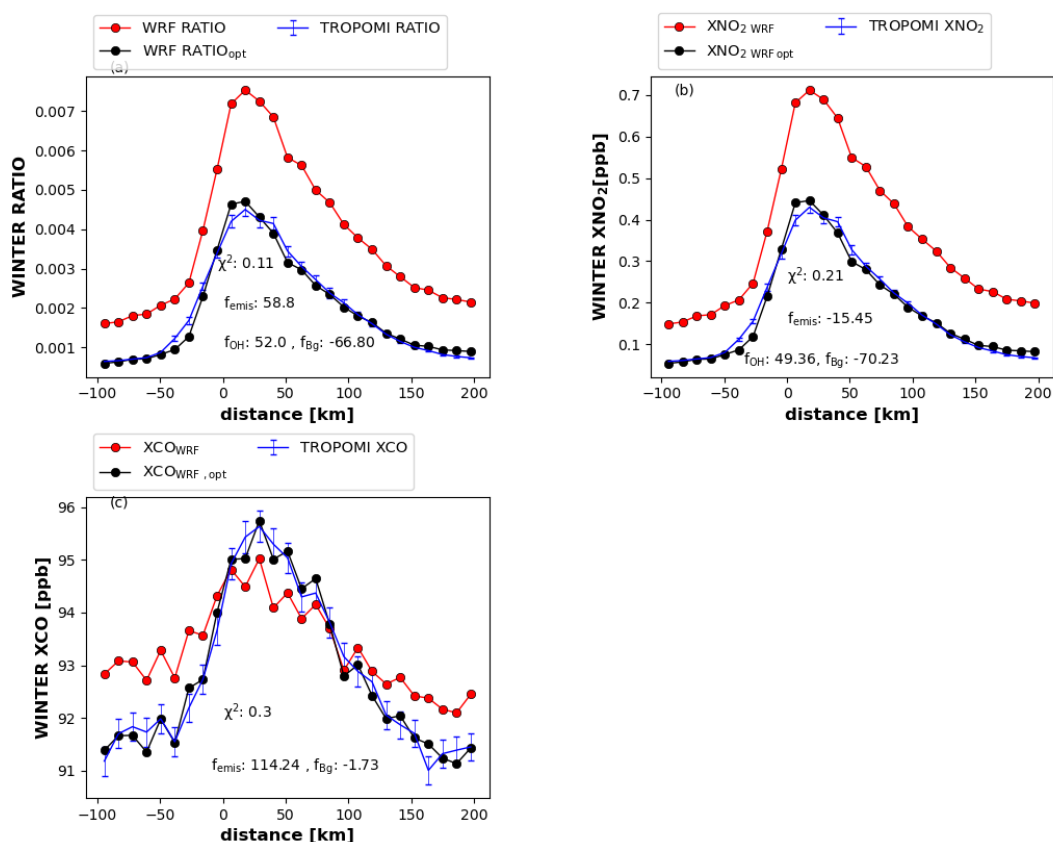


Figure 5. As Figure 4, for Winter (averaged over November, 2018 to March, 2019)

Figure 4a shows WRF ratios for summer in comparison to TROPOMI, before and after optimizing the OH concentration. The optimized WRF ratios fit the TROPOMI ratios well with $X^2 = 0.1$ (for the derivation of X^2 see section S4). The estimated uncertainties for the scaling factors f_{emis} , f_{OH} and f_B are derived by summing the contribution of wind speed, length and width of box and NO_2 bias correction in quadrature as provided in Tables S1 and S2. For summer and winter, the uncertainties of the optimized OH concentrations range from 11 % to 15 %. For NO_x and CO emissions, these uncertainty ranges are ~25 % and ~10 to 15 %, respectively. According to the ratio optimization, the CAMS OH and the emission ratio are underestimated by 32.03 ± 4.0 % and 155.1 ± 14.9 % respectively. The CAMS background ratio is overestimated by 70.1 ± 6.2 %. It should be realized here that the ratio optimization does not estimate the absolute emission of NO_2 and CO, but only their ratio.

To investigate the implication of this, we performed component-wise optimizations of WRF-derived XCO_{WRF} and $XNO_{2,WRF}$. Optimized XCO_{WRF} and $XNO_{2,WRF}$ fit well to the TROPOMI data (see Fig. 4b and 4c). In the XNO_2 optimization, the EDGAR NO_x emission is increased by 42.1 ± 9.5 % and the CAMS background is reduced by 75.92 ± 10.0 %. OH is increased by 28.3 ± 3.7 %, close to the results obtained from the ratio optimization. In the XCO optimization, EDGAR CO emissions are roughly doubled and the background is reduced by 4.55 ± 0.5 % compared to CAMS. The ratio optimization suggests to increase the prior emission ratio 0.68 by 155.1 %. The summer optimized NO_x/CO emission ratio derived from the component wise optimization is 0.38. The optimized emission ratio from ratio optimization is larger by factor 4.7 compared to component wise optimization. The difference between two estimates can be explained by different constraints on the solution in the two methods. In particular, the ratio inversion allows emission adjustment in a fixed relation between NO_2 and CO emissions whereas the component wise has the full flexibility to adjust CO and NO_2 emission. The difference between the two estimates is larger than expected but does not affect the OH estimation. Lama et al., (2020) calculated TROPOMI derived summer emission (NO_2/CO) ratio for 2018 over Riyadh and mentioned that Monitoring Atmospheric Chemistry and Climate and CityZen (MACCity) emission ratio is more consistent with the TROPOMI derived ratio than EDGAR. The optimized emission ratio obtained from component wise optimization is consistent to Lama et al., (2020) and MACCity summer emissions. This shows that for the accurate estimation of the emission and emission ratio, the component wise optimization method is preferable.

Figure 5 presents optimization results for winter, where optimized WRF is in similar good agreement with TROPOMI as for summer with $X^2 = 0.11$. For winter, the ratio optimization increases OH by 52.0 ± 5.3 % and the emission ratio by 58.8 ± 30.2 %. The ratio and component-wise optimizations again show similar OH adjustments, demonstrating the robustness of our method. The background ratio is reduced by 66.80 ± 5.8 %. The component-wise optimization for XNO_2 reduces the EDGAR NO_x emission by 15.45 ± 3.4 % and the CAMS background by 70.23 ± 6.1 %. For XCO , the WRF XCO_{Bg} is reduced by 1.73 ± 0.1 % in combination with a doubling of the EDGAR CO emission. The optimized emission ratio (NO_x/CO) derived from component wise optimization is 0.33 which is lower by 3.5 times than optimized emission ratio obtained from ratio optimization.

Table 2. Overview of WRF optimized OH and NO_x emissions for Riyadh and comparison to the EMG method. The estimated uncertainty for EMG and WRF derived NO_x emission and OH concentration is the sum of the contribution of wind speed, length and width of box and NO₂ bias correction provided in Table S1, S2 and S3.

| Parameter | Summer WRF Optimization | | Summer EMG | Winter WRF Optimization | | Winter EMG |
|--|----------------------------|-----------|---------------|----------------------------|------------|---------------|
| | Prior | After | | Prior | After | |
| NO_x emission (kg/second) | 8.2 | 11.6±2.4 | 8.6±1.2 | 9.4 | 7.9±1.8 | 5.3±1.5 |
| OH (1e⁷, molecules/cm³) | 1.3 | 1.7 ± 0.2 | 1.4 ± 0.2 | 0.86 | 1.3 ± 0.14 | 1.2 ± 0.1 |
| NO_x lifetime (hr) | 3.1 | 2.4 ± 0.4 | 2.9 ± 0.3 | 4.9 | 3.3 ± 0.3 | 3.6 ± 0.3 |

To investigate the consistency between our method and the EMG method, the derived NO_x lifetimes, emissions and OH concentrations using both methods are listed in Table 2 for winter and summer. Our optimization and the EMG method agree well on the seasonal change in NO_x emission and OH concentration. Both methods result in higher NO_x emissions and shorter lifetimes in summer; lower NO_x emissions and longer lifetimes in winter. Riyadh has a dry and warm summer days and the increase in power consumption due to the use of air conditioning contributes to the higher emission in summer than in winter (Lange et al., 2021). During the summer, EMG and the WRF optimization method both increase the NO_x emission and OH concentration compared with the prior. The size of the NO_x emission and OH concentration increase, obtained using the WRF optimization method is higher than the EMG method by 15% to 29%. However, the difference between the EMG method and the component optimization method are smaller compared to the uncertainty of the emission and OH concentration derived for the optimization method. For winter, the dissimilarity between the EMG method and the prior reduces after optimization. The NO_x emission after optimization differs from the EMG method by 33%. Optimized OH concentration and NO_x lifetime differs by <10% compared to EMG method. In general, the difference between the EMG and optimization results is within the uncertainty range of 20 to 30%, confirming their consistency and strengthening the confidence in the estimates that are obtained from TROPOMI data.

In contrast to EMG method, the optimization method can be used for a single TROPOMI overpass and does not require yearly averaged NO₂ data. Segregation and averaging of NO₂ urban plume by wind sector is not required in the optimization method. The effect of transport cancels out in taking the NO₂ / CO ratio and loss of NO₂ is mostly governed by OH. In this study, NO_x emission and OH concentration is estimated iteratively whereas the EMG method arrives at the solution in a single step. However, since our optimization method requires a WRF model simulation it is computationally more expensive. Uncertainties in transport may create mismatches with the satellite observations, leading to errors in the optimized fit. This influences the quality of derived emission estimates (Dekker et al., 2017). Therefore, finding a simplified approach using satellite data to derive the emission ratio and to estimate OH concentration in urban plumes will be our focus in the future.

It should be realized that the a priori EDGAR emissions and TROPOMI optimized estimates represent different years (2012 and 2018, respectively). To check whether the emission differences that are found may be explained by trends in emissions, we compare EDGAR 2012 NO_x and CO emissions with 2018 accounting for seasonal and diurnal emission variations using temporal emission factors by van der Gon et al., (2011). EDGAR 2018 NO_x and CO emissions are derived by linear extrapolation using emission from 2000 to 2015 (see Figure S19). For summer mid-day NO_x emissions, the EDGAR emissions increased by 17.7% from 2012 to 2018, which is lower than our optimization results. For winter, mid-day NO_x emissions increase in EDGAR by 13% from 2012 to 2018, whereas the WRF optimization yield reductions by 15.6%. In EDGAR, summer and winter CO emissions increased from 2012

to 2018 by 25.5 % and 20.0 %, respectively. However, the WRF optimization suggests that the EDGAR CO emissions for summer and winter need to be doubled (see Table S4). Borsdorff et al., (2018) mentioned that EDGAR CO emissions has to be increased significantly to match with TROPOMI CO observations over middle eastern cities such as Tehran, Yerevan, Tabriz and Urmia. Overall , this points to a significant uncertainty in the EDGAR emission inventory at the city scale.

To test the accuracy of the linear extrapolation of EDGAR data, we compare the relative change in NO_x and CO emission in 2012 to 2018 using CAMS Global (CAMS–GLOB) anthropogenic v4.2 emission datasets (<https://ads.atmosphere.copernicus.eu/cdsapp#!/dataset/cams-global-emission-inventories?tab=overview>). CAMS – GLOB shows that for summer and winter NO_x emission increases by 26 % from 2012 to 2018, which is higher by a factor 2 than EDGAR. CAMS-GLOB based summer and winter CO emission increases by 20 % from 2012 to 2018 which differs by ~20 % compared to EDGAR. In general, the relative increase in CO and NO_x emission from EDGAR and CAMS-GLOB is much smaller compared to the difference with our optimization method.

We realise that our method only considers the first order loss of NO₂ by OH forming HNO₃. In reality, the NO₂ lifetime is influenced by more spatially and temporally varying factors such as temperature, ozone, and radiation (Lang et al., 2015; Romer et al., 2018). In cities, the loss of NO₂ via the formation of alkyl and multifunctional nitrates (RONO₂) are also important reactions influencing the lifetime of NO₂ (Browne et al., 2013; Sobanski et al., 2017). For CO, secondary production from short-lived volatile organic compounds can also play an important role in urban pollution plumes. The application of full chemistry that includes all the sources and losses of NO₂ and CO could therefore further improve the accuracy of OH estimates.

Another complicating factor is the strong variation in chemical regime that is expected in city air pollution plumes. Close to high NO_x sources, OH tends to be titrated away by the NO₂ (Valin et al., 2011). Further from the source, chemical conditions may be favorable for OH formation and recycling, reducing the NO₂ lifetime. To investigate this in order to refine the OH estimates presented in this paper, again a full chemistry framework would be required.

Figure S20 shows that power plants and manufacturing industries are the largest pollutant emitter over Riyadh (Beirle et al., 2019). In this study, NO_x and CO anthropogenic emissions are introduced at the surface, whereas the emission height of different sources is expected to vary in reality. The different emission heights for NO_x and CO emission sources can also influence the result. In the future, realistic emission heights should also be incorporated in WRF for accurate estimation of OH. Moreover, the temporal emission factors that have been used by van der Gon et al., (2011) are based on European countries. The comparison of van der Gon et al., (2011) with the Copernicus Atmosphere Monitoring Service TEMPO profiles (CAMS-TEMPO) suggests that temporal emission factors for weekend road transport and monthly residential combustion are different in Riyadh compared to European countries. Road transport, CO emission has the largest contribution ~75 % to the total emission over Riyadh, whereas NO_x emission from road contributes by 24% to the total NO_x emission. Residential combustion has the smallest contribution of ~0.3 to 0.4 % to total NO_x and CO emissions (see Fig S20). In the future, the application of accurate diurnal emission factors for road transport can further improve the accuracy of urban OH concentrations estimated using TROPOMI derived XNO₂/XCO ratios. In addition, the seasonality for NO_x and CO emissions is different in Riyadh than in Europe, which should be accounted for in future studies also.

5 Conclusions

In this study, a new method is presented for estimating OH concentrations in urban plumes using TROPOMI observed XNO₂/XCO ratios in combination with WRF simulations of the downwind pollution plume of large cities. Our new method has been tested for the city of Riyadh using synthetic as well as real TROPOMI data. Seasonal emissions and OH concentrations have been estimated for summer (June to October, 2018) and winter (Nov, 2018 to March, 2019).

WRF is well able to reproduce the spatial distribution of TROPOMI retrieved XNO_2 and XCO plumes over Riyadh during the summer and winter seasons. However, the TROPOMI observed level of XNO_2 is lower than simulated using WRF by 25 % in summer and 40 to 50 % in winter. In both seasons, TROPOMI XCO agrees within 10 % with WRF. The variation in XNO_2 , XCO and their ratio as a function of downwind distance to the centre of Riyadh agrees well between WRF and TROPOMI. However, the WRF derived XNO_2/XCO ratio is higher by 15% to 30 % in summer and 49 % in winter compared to TROPOMI, explained mostly by the difference in XNO_2 .

The differences between WRF and TROPOMI observations have been used to optimize emissions and the NO_2 lifetime. To this end, scaling factors for the city emissions, OH and the background level have been optimized iteratively using a least squares method. Ratio and component wise optimizations have been compared to test the overall consistency of the method. In summer, the ratio and XNO_2 optimization for XNO_2 suggest that the OH prior from CAMS is underestimated by $32.03 \pm 4.0\%$. Estimates obtained from the ratio and NO_2 -only optimization agree within 10 %, demonstrating the robustness of the method. Summertime emissions of NO_x and CO from EDGAR are increased by $42.1 \pm 8.7\%$ and $100.8 \pm 9.5\%$. For winter, the ratio and component wise optimizations increase OH by $\sim 52.0 \pm 5.3\%$ to fit TROPOMI inferred ratios. In the optimization of winter data, NO_x emissions are reduced by $15.45 \pm 3.4\%$ and CO emissions are doubled. In the future, the remaining differences between TROPOMI observations and WRF simulations could be reduced further by the use of precise temporal and monthly emission factors, emission heights and full chemistry to account for secondary sources of CO and NO_2 .

TROPOMI inferred OH concentrations obtained from the least squares optimization method have been compared to the EMG method. For the summer, the optimized OH concentrations differ by 18 %, whereas they are within 7.5 % during winter. These results confirm that urban emissions and OH concentrations can robustly be estimated from TROPOMI data. With our method, single TROPOMI overpass can be used to estimate OH whereas EMG method requires averaging of NO_2 urban plume by wind sector. The iterative approach allows to test the factors i.e. f_{emis} , f_{oh} and f_{bg} obtained from optimization method, whereas EMG method does not allow such flexibility.

An important remaining uncertainty is the bias correction of the TROPOMI XNO_2 retrieval. Following the recommended procedure, the air mass factor AMF is recalculated by replacing the tropospheric AMF based on TM5, that is provided with the data, with WRF-chem. The TROPOMI XNO_2 bias correction increases the mixing ratio in the urban plume of Riyadh by 5 to 10 % in summer and 25 to 30 % in winter. The background is less affected by the bias correction. Without TROPOMI XNO_2 bias correction, the uncertainty in scaling factor for OH can vary up to 20 % and NO_x emission to 60 % over Riyadh.

Appendix A: NO_2 bias correction

The air mass factor (AMF) used in the retrieval of TROPOMI XNO_2 has been re-calculated by replacing the tropospheric AMF, calculated from the NO_2 column simulated by TM5, with its WRF-chem equivalent, as described by Lamsal et al. (2010) and Boersma et al. (2016) using the following equation,

$$M_{\text{trop, WRF}} = M_{\text{trop, TM5}} \times \frac{\sum_{l=1}^L A_{\text{trop},l} x_{l,\text{WRF}}}{\sum_{l=1}^L x_{l,\text{WRF}}} \quad (16)$$

where, $M_{\text{trop,WRF}}$ and $M_{\text{trop,TM5}}$ are the tropospheric air mass factors derived from WRF and TM5, respectively. $A_{\text{trop},l}$ is the tropospheric averaging kernel, ranging from the surface to the uppermost layer of the troposphere in the TM5 model (l). $x_{l,\text{WRF}}$ is the equivalent NO_2 column density in model layer l, based on WRF. A_{trop} in equation 16 is derived using $A_{\text{trop}} = A \times \frac{M}{M_{\text{trop}}}$, where M and M_{trop} are the total and tropospheric AMF's respectively. Finally, the bias corrected NO_2 vertical column density is computed using,

$$\text{NO}_{2, \text{ bias corrected}} = \frac{M_{\text{trop, TM5}}}{M_{\text{trop, WRF}}} \times \text{NO}_2$$

where, NO_2 is the TROPOMI tropospheric NO_2 vertical column density and $\text{NO}_{2, \text{ bias corrected}}$ is the bias corrected TROPOMI tropospheric NO_2 vertical column density.

Appendix B

The component wise optimization of XCO_{WRF} to estimate the emission and background of CO uses the following equation,

$$\text{XCO}_{\text{TROPOMI}} = \text{XCO}_{\text{WRF}} + \Delta\text{XCO}_{\text{emis}} * \frac{f_{\text{emis}}}{10} + \Delta\text{XCO}_{\text{Bg}} * \frac{f_{\text{Bg}}}{10}$$

$$\text{XCO}_{\text{WRF}} = \text{XCO}_{\text{emis}} + \text{XCO}_{\text{Bg}}$$

$$\Delta\text{XCO}_{\text{emis}} = \text{XCO}_{\text{emis}} * 1.10 - \text{XCO}_{\text{emis}}$$

$$\Delta\text{XCO}_{\text{Bg}} = \text{XCO}_{\text{Bg}} * 1.10 - \text{XCO}_{\text{Bg}}$$

Here, $\text{XCO}_{\text{TROPOMI}}$ is TROPOMI XCO, XCO_{WRF} is the WRF simulated XCO accounting for emissions and background CO, XCO_{emis} is the XCO contribution from the urban CO emission and XCO_{Bg} is the CAMS-derived XCO background. $\Delta\text{XCO}_{\text{emis}}$ is the change in XCO due to emission and $\Delta\text{XCO}_{\text{Bg}}$ is the change in the XCO background level.

Acknowledgments

We are thankful to the team that designed the TROPOMI instrument, consisting of the partnership between Airbus Defence and Space Netherlands, KNMI, SRON, and TNO, commissioned by NSO and ESA. This work is supported by NWO GO programme (grant no. 2017.036). We acknowledge the free availability of WRF-Chem model (<http://www.wrf-model.org/>). Thanks to SURFSara for making the Cartesius HPC platform available for computations via computing grant no. 17235.

Data Availability Statement

TROPOMI CO and NO_2 data can be downloaded from <https://cophub.copernicus.eu/s5pexp>. EDGAR emission data is available at https://edgar.jrc.ec.europa.eu/emissions_data_and_maps. CAMS data can be downloaded from <https://ads.atmosphere.copernicus.eu/cdsapp#!/dataset/cams-global-reanalysis-eac4?tab=form>. WRF simulations output are available at <https://zenodo.org/deposit?page=1&size=20>

References

- Babic, L., Braak, R., Dierssen, R., Kissi-Ameyaw, J., Kleipool, J., Leloux, J., Loots, E., Ludewig, A., Rozemeijer, N., Smeets, S., and Vacanti, G. (2017). Algorithm theoretical basis document for the TROPOMI L01b data processor Erwin Loots Quintus Kleipool.
- Beirle, S., Boersma, K. F., Platt, U., Lawrence, M. G., & Wagner, T. (2011a). Megacity emissions and lifetimes of nitrogen oxides probed from space. *Science*, 333(6050), 1737–1739. <https://doi.org/10.1126/science.1207824>
- Beirle, S., Boersma, K. F., Platt, U., Lawrence, M. G., & Wagner, T. (2011b). Megacity emissions and lifetimes of nitrogen oxides probed from space. *Science*, 333(6050), 1737–1739. <https://doi.org/10.1126/science.1207824>
- Beirle, S., Borger, C., Dörner, S., Li, A., Hu, Z., Liu, F., et al. (2019a). Pinpointing nitrogen oxide emissions from space. *Science Advances*, 5(11), 1–7. <https://doi.org/10.1126/sciadv.aax9800>

- Beirle, S., Borger, C., Dörner, S., Li, A., Hu, Z., Liu, F., et al. (2019b). Pinpointing nitrogen oxide emissions from space. *Science Advances*, 5(11).
<https://doi.org/10.1126/sciadv.aax9800>
- Boersma, K. F., Vinken, G. C. M., & Eskes, H. J. (2016). Representativeness errors in comparing chemistry transport and chemistry climate models with satellite UV-Vis tropospheric column retrievals. *Geoscientific Model Development*, 9(2), 875–898.
<https://doi.org/10.5194/gmd-9-875-2016>
- Boersma, K. Folkert, Eskes, H. J., Richter, A., De Smedt, I., Lorente, A., Beirle, S., et al. (2018). Improving algorithms and uncertainty estimates for satellite NO₂ retrievals: Results from the quality assurance for the essential climate variables (QA4ECV) project. *Atmospheric Measurement Techniques*, 11(12), 6651–6678. <https://doi.org/10.5194/amt-11-6651-2018>
- Borsdorff, T., Hasekamp, O. P., Wassmann, A., & Landgraf, J. (2014). Insights into Tikhonov regularization: Application to trace gas column retrieval and the efficient calculation of total column averaging kernels. *Atmospheric Measurement Techniques*, 7(2), 523–535.
<https://doi.org/10.5194/amt-7-523-2014>
- Borsdorff, T., Aan de Brugh, J., Hu, H., Aben, I., Hasekamp, O., & Landgraf, J. (2018). Measuring Carbon Monoxide With TROPOMI: First Results and a Comparison With ECMWF-IFS Analysis Data. *Geophysical Research Letters*, 45(6), 2826–2832.
<https://doi.org/10.1002/2018GL077045>
- Borsdorff, Tobias, Andrasec, J., De Brugh, J. A., Hu, H., Aben, I., & Landgraf, J. (2018). Detection of carbon monoxide pollution from cities and wildfires on regional and urban scales: the benefit of CO column retrievals from SCIAMACHY 2.3 μm measurements under cloudy conditions. *Atmospheric Measurement Techniques*, 11(5), 2553–2565.
<https://doi.org/10.5194/amt-11-2553-2018>
- Borsdorff, Tobias, Aan De Brugh, J., Hu, H., Hasekamp, O., Sussmann, R., Rettinger, M., et al. (2018). Mapping carbon monoxide pollution from space down to city scales with daily global coverage. *Atmospheric Measurement Techniques*, 11(10), 5507–5518.
<https://doi.org/10.5194/amt-11-5507-2018>
- Borsdorff, Tobias, Aan De Brugh, J., Pandey, S., Hasekamp, O., Aben, I., Houweling, S., & Landgraf, J. (2019). Carbon monoxide air pollution on sub-city scales and along arterial roads detected by the Tropospheric Monitoring Instrument. *Atmospheric Chemistry and Physics*, 19(6), 3579–3588. <https://doi.org/10.5194/acp-19-3579-2019>
- Browne, E. C., Min, K. E., Wooldridge, P. J., Apel, E., Blake, D. R., Brune, W. H., et al. (2013). Observations of total RONO₂ over the boreal forest: NO_x sinks and HNO₃ sources. *Atmospheric Chemistry and Physics*. <https://doi.org/10.5194/acp-13-4543-2013>
- Crippa, M., Janssens-Maenhout, G., Dentener, F., Guizzardi, D., Sindelarova, K., Muntean, M., et al. (2016). Forty years of improvements in European air quality: Regional policy-industry interactions with global impacts. *Atmospheric Chemistry and Physics*.
<https://doi.org/10.5194/acp-16-3825-2016>
- Crippa, M., Solazzo, E., Huang, G., Guizzardi, D., Koffi, E., Muntean, M., et al. (2020). High resolution temporal profiles in the Emissions Database for Global Atmospheric Research. *Scientific Data*, 7(1), 1–17. <https://doi.org/10.1038/s41597-020-0462-2>

- Dekker, I. N., Houweling, S., Aben, I., Röckmann, T., Krol, M., Martínez-Alonso, S., et al. (2017). Quantification of CO emissions from the city of Madrid using MOPITT satellite retrievals and WRF simulations. *Atmospheric Chemistry and Physics*, 17(23), 14675–14694. <https://doi.org/10.5194/acp-17-14675-2017>
- Ding, J., Miyazaki, K., Van Der A, R. R., Mijling, B., Kurokawa, J. I., Cho, S. Y., et al. (2017). Intercomparison of NO_x emission inventories over East Asia. *Atmospheric Chemistry and Physics*, 17(16), 10125–10141. <https://doi.org/10.5194/acp-17-10125-2017>
- Ek, M. B., Mitchell, K. E., Lin, Y., Rogers, E., Grunmann, P., Koren, V., et al. (2003). Implementation of Noah land surface model advances in the National Centers for Environmental Prediction operational mesoscale Eta model. *Journal of Geophysical Research: Atmospheres*, 108(22), 1–16. <https://doi.org/10.1029/2002jd003296>
- Eskes, H.J., van Geffen, J., Boersma, K.F., Eichmann, K.-U., Apituley, A., Pedernana, M., Sneep, M., Pepijn, J., Loyola, D. (2018). Level 2 Product User Manual Henk Eskes.
- Flagan, R. C., & Seinfeld, J. H. (1988). *Fundamentals of Air Pollution Engineering*. *Fundamentals of Air Pollution*.
- van Geffen, J. H. G. M., Eskes, H. J., Boersma, K. F., Maasakkers, J. D., & Veefkind, J. P. (2019). TROPOMI ATBD of the total and tropospheric NO₂ data products, S5P-KNMI-L2-0005-RP, issue 1.4.0, 6 February 2019. *S5P-Knmi-L2-0005-Rp*, (1.4.0), 1–76. Retrieved from <https://sentinel.esa.int/documents/247904/2476257/Sentinel-5P-TROPOMI-ATBD-NO2-data-products>
- Georgoulias, A. K., Van Der, R. A. J., Stammes, P., Folkert Boersma, K., & Eskes, H. J. (2019). Trends and trend reversal detection in 2 decades of tropospheric NO₂ satellite observations. *Atmospheric Chemistry and Physics*, 19(9), 6269–6294. <https://doi.org/10.5194/acp-19-6269-2019>
- van der Gon, H. D., Hendriks, C., Kuenen, J., Segers, A., & Visschedijk, A. (2011). TNO Report: Description of current temporal emission patterns and sensitivity of predicted AQ for temporal emission patterns, (December), 1–22.
- de Gouw, J. A., Parrish, D. D., Brown, S. S., Edwards, P., Gilman, J. B., Graus, M., et al. (2019). Hydrocarbon Removal in Power Plant Plumes Shows Nitrogen Oxide Dependence of Hydroxyl Radicals. *Geophysical Research Letters*, 0–2. <https://doi.org/10.1029/2019GL083044>
- Grell, G. A., Peckham, S. E., Schmitz, R., McKeen, S. A., Frost, G., Skamarock, W. C., & Eder, B. (2005). Fully coupled “online” chemistry within the WRF model. *Atmospheric Environment*, 39(37), 6957–6975. <https://doi.org/10.1016/j.atmosenv.2005.04.027>
- Hong, S., & Lim, J. (2006). HongandLim_JKMS_WSM6_2006. *Journal of the Korean Meteorological Society*. Retrieved from http://www.mmm.ucar.edu/wrf/users/docs/WSM6-hong_and_lim_JKMS.pdf 5Cnhttp://search.koreanstudies.net/journal/thesis_name.asp?tna=me=kiss2002&key=2525908
- Hu, X. M., Klein, P. M., & Xue, M. (2013). Evaluation of the updated YSU planetary boundary layer scheme within WRF for wind resource and air quality assessments. *Journal of Geophysical Research Atmospheres*, 118(18), 10,490–10,505. <https://doi.org/10.1002/jgrd.50823>

- Huijnen, V., Pozzer, A., Arteta, J., Brasseur, G., Bouarar, I., Chabrillat, S., et al. (2019). Quantifying uncertainties due to chemistry modelling - Evaluation of tropospheric composition simulations in the CAMS model (cycle 43R1). *Geoscientific Model Development*, 12(4), 1725–1752. <https://doi.org/10.5194/gmd-12-1725-2019>
- Ialongo, I., Virta, H., Eskes, H., Hovila, J., & Douros, J. (2020). Comparison of TROPOMI/Sentinel-5 Precursor NO₂ observations with ground-based measurements in Helsinki. *Atmospheric Measurement Techniques*, 13(1), 205–218. <https://doi.org/10.5194/amt-13-205-2020>
- Inness, A., Ades, M., Agustí-Panareda, A., Barr, J., Benedictow, A., Blechschmidt, A. M., et al. (2019). The CAMS reanalysis of atmospheric composition. *Atmospheric Chemistry and Physics*, 19(6), 3515–3556. <https://doi.org/10.5194/acp-19-3515-2019>
- Krol, M., Houweling, S., Bregman, B., Broek, M. Van Den, Segers, A., Velthoven, P. Van, et al. (2005). and Physics The two-way nested global chemistry-transport zoom model TM5 : algorithm and applications. *Atmospheric Chemistry and Physics*, 417–432.
- Lama, S., Houweling, S., Folkert Boersma, K., Eskes, H., Aben, I., A. C. Denier Van Der Gon, H., et al. (2020). Quantifying burning efficiency in megacities using the NO₂•CO ratio from the Tropospheric Monitoring Instrument (TROPOMI). *Atmospheric Chemistry and Physics*, 20(17), 10295–10310. <https://doi.org/10.5194/acp-20-10295-2020>
- Lambert, J.-C., A. Keppens, D. Hubert, B. Langerock, K.-U. Eichmann, Q. Kleipool, M. Sneep, T. Verhoelst, T. Wagner, M. Weber, C. Ahn, A. Argyrouli, D. Balis, K.L. Chan, S. Compennolle, I. De Smedt, H. Eskes, A.M. Fjæraa, K. Garane, J.F. Gleason, F. Gouta, and P. W. (2019). Sentinel-5 Precursor Mission Performance Centre Quarterly Validation Report of the Copernicus Sentinel-5 Precursor Operational Data Products # 03 : July 2018 – May 2019, 1–125.
- Lamsal, L. N., Martin, R. V., Van Donkelaar, A., Celarier, E. A., Bucsela, E. J., Boersma, K. F., et al. (2010). Indirect validation of tropospheric nitrogen dioxide retrieved from the OMI satellite instrument: Insight into the seasonal variation of nitrogen oxides at northern midlatitudes. *Journal of Geophysical Research Atmospheres*, 115(5), 1–15. <https://doi.org/10.1029/2009JD013351>
- Landgraf, J., Aan De Brugh, J., Scheepmaker, R., Borsdorff, T., Hu, H., Houweling, S., et al. (2016). Carbon monoxide total column retrievals from TROPOMI shortwave infrared measurements. *Atmospheric Measurement Techniques*, 9(10), 4955–4975. <https://doi.org/10.5194/amt-9-4955-2016>
- Lang, M. N., Gohm, A., & Wagner, J. S. (2015). The impact of embedded valleys on daytime pollution transport over a mountain range. *Atmospheric Chemistry and Physics*. <https://doi.org/10.5194/acp-15-11981-2015>
- Lange, K., Richter, A., & Burrows, J. P. (2021). Variability of nitrogen oxide emission fluxes and lifetimes estimated from Sentinel-5P TROPOMI observations. *Atmospheric Chemistry and Physics Discussions*, 2(2), 1–32. <https://doi.org/10.5194/acp-2021-273>
- Liu, F., Beirle, S., Zhang, Q., Dörner, S., He, K., & Wagner, T. (2016). NO_x lifetimes and emissions of cities and power plants in polluted background estimated by satellite observations. *Atmospheric Chemistry and Physics*, 16(8), 5283–5298.

<https://doi.org/10.5194/acp-16-5283-2016>

- Lorente, A., Boersma, K. F., Eskes, H. J., Veefkind, J. P., van Geffen, J. H. G. M., de Zeeuw, M. B., et al. (2019a). Quantification of nitrogen oxides emissions from build-up of pollution over Paris with TROPOMI. *Scientific Reports*, 9(1), 1–10. <https://doi.org/10.1038/s41598-019-56428-5>
- Lorente, A., Boersma, K. F., Eskes, H. J., Veefkind, J. P., van Geffen, J. H. G. M., de Zeeuw, M. B., et al. (2019b). Quantification of nitrogen oxides emissions from build-up of pollution over Paris with TROPOMI. *Scientific Reports*. <https://doi.org/10.1038/s41598-019-56428-5>
- Lorente, Alba, Folkert Boersma, K., Yu, H., Dörner, S., Hilboll, A., Richter, A., et al. (2017). Structural uncertainty in air mass factor calculation for NO₂ and HCHO satellite retrievals. *Atmospheric Measurement Techniques*, 10(3), 759–782. <https://doi.org/10.5194/amt-10-759-2017>
- M. Tewari, F. Chen, W. Wang, J. Dudhia, M. A. L., K. Mitchell, M. Ek, G. G., & National, J. W. R. H. C. (n.d.). Clay. In: *The Conference on Weather Analysis and Forecasting*.
- Mlawer, E. J., Taubman, S. J., Brown, P. D., Iacono, M. J., & Clough, S. A. (1997). Radiative transfer for inhomogeneous atmospheres: RRTM, a validated correlated-k model for the longwave. *Journal of Geophysical Research Atmospheres*, 102(14), 16663–16682. <https://doi.org/10.1029/97jd00237>
- Pascal, M., Corso, M., Chanel, O., Declercq, C., Badaloni, C., Cesaroni, G., et al. (2013). Assessing the public health impacts of urban air pollution in 25 European cities: Results of the Aphekom project. *Science of the Total Environment*, 449(2007105), 390–400. <https://doi.org/10.1016/j.scitotenv.2013.01.077>
- Pommier, M., McLinden, C. A., & Deeter, M. (2013). Relative changes in CO emissions over megacities based on observations from space. *Geophysical Research Letters*, 40(14), 3766–3771. <https://doi.org/10.1002/grl.50704>
- Romer, P. S., Duffey, K. C., Wooldridge, P. J., Edgerton, E., Baumann, K., Feiner, P. A., et al. (2018). Effects of temperature-dependent NO_x emissions on continental ozone production. *Atmospheric Chemistry and Physics*. <https://doi.org/10.5194/acp-18-2601-2018>
- Sannigrahi, S., Kumar, P., Molter, A., Zhang, Q., Basu, B., Basu, A. S., & Pilla, F. (2021). Examining the status of improved air quality in world cities due to COVID-19 led temporary reduction in anthropogenic emissions. *Environmental Research*, 196(September 2020), 110927. <https://doi.org/10.1016/j.envres.2021.110927>
- Sicard, P., Agathokleous, E., De Marco, A., Paoletti, E., & Calatayud, V. (2021). Urban population exposure to air pollution in Europe over the last decades. *Environmental Sciences Europe*, 33(1). <https://doi.org/10.1186/s12302-020-00450-2>
- Sobanski, N., Thieser, J., Schuladen, J., Sauvage, C., Song, W., Williams, J., et al. (2017). Day and night-time formation of organic nitrates at a forested mountain site in south-west Germany. *Atmospheric Chemistry and Physics*. <https://doi.org/10.5194/acp-17-4115-2017>
- United Nations. (2018). *World Urbanization Prospects. Demographic Research* (Vol. 12). <https://doi.org/10.4054/demres.2005.12.9>
- Valin, L. C., Russell, A. R., Hudman, R. C., & Cohen, R. C. (2011). Effects of model resolution

- on the interpretation of satellite NO₂ observations. *Atmospheric Chemistry and Physics*, 11(22), 11647–11655. <https://doi.org/10.5194/acp-11-11647-2011>
- Valin, L. C., Russell, A. R., & Cohen, R. C. (2013). Variations of OH radical in an urban plume inferred from NO₂ column measurements. *Geophysical Research Letters*. <https://doi.org/10.1002/grl.50267>
- Veefkind, J. P., Aben, I., McMullan, K., Förster, H., de Vries, J., Otter, G., et al. (2012). TROPOMI on the ESA Sentinel-5 Precursor: A GMES mission for global observations of the atmospheric composition for climate, air quality and ozone layer applications. *Remote Sensing of Environment*. <https://doi.org/10.1016/j.rse.2011.09.027>
- Verstraeten, W. W., Boersma, K. F., Douros, J., Williams, J. E., Eskes, H., Liu, F., et al. (2018). Top-down NO_x emissions of european cities based on the downwind plume of modelled and space-borne tropospheric NO₂ columns. *Sensors (Switzerland)*, 18(9). <https://doi.org/10.3390/s18092893>
- Visser, A. J., Folkert Boersma, K., Ganzeveld, L. N., & Krol, M. C. (2019). European NO_x emissions in WRF-Chem derived from OMI: Impacts on summertime surface ozone. *Atmospheric Chemistry and Physics*, 19(18), 11821–11841. <https://doi.org/10.5194/acp-19-11821-2019>
- Wennberg, P. O., Stremme, W., Schneider, M., Feist, D. G., aan de Brugh, J., Toon, G. C., et al. (2018). Mapping carbon monoxide pollution from space down to city scales with daily global coverage. *Atmospheric Measurement Techniques*, 11(10), 5507–5518. <https://doi.org/10.5194/amt-11-5507-2018>
- Zhang, C., & Wang, Y. (2017). Projected future changes of tropical cyclone activity over the Western North and South Pacific in a 20-km-Mesh regional climate model. *Journal of Climate*, 30(15), 5923–5941. <https://doi.org/10.1175/JCLI-D-16-0597.1>